List of Abbreviations

TMO	Transition metal oxide
SMO	Semi-conductor metal oxide
Cu	Copper
CuO_x	Copper oxide
Cu_2O	Cuprous oxide
CuO	Cupric oxide
Zn	Zinc
ZnO	Zinc oxide
TiO_2	Titanium dioxide
SnO_2	Tin dioxide
Bi_2O_3	Bismuth trioxide
NiO	Nickel (II) Oxide
Ta	Tantalum
Mo	Molybdenum
W	Tungsten
Ag	Silver
Ti	Titanium
CO	Carbon monoxide
He	Helium
O_2	Oxygen
Ar	Argen
N_2	Nitrogen
MB	Methylene blue
HH	Hydrogen Hydrate
RT	Room Temperature
RF	Radio Frequency
DC	Direct Current
PVD	Physical vapor deposition
CVD	Chemical vapour deposition
PLD	Pulsed laser deposition
MBE	Molecular beam epitaxy

XRD	X-ray diffraction
SEM	Scanning electron microscopy
XPS	X-ray photoemission spectroscopy
UV-Vis	Ultraviolet-visible
AFM	Atomic force microscopy
STM	Scanning tunneling microscopy
XPS	X -ray photoemission spectroscopy
EDS	Energy dispersive Spectroscopy
SPSTM	Spin polarized scanning tunneling microscope
BEEM	Ballistic electron emission microscope
SFEM	Scanning field emission microscope
PSPD	Position sensitive photo-detector
PID	Proportional–integral–derivative
DMHCS	Disordered mesoporous carbon spheres
LED	Light emitting diodes
US-NIOSH	United States National Institute of Occupational Safety and Health
PQMS	Physical quantity measurement system
JCPDS	Joint Committee on Powder Diffraction Standards
FWHM	Full-width half maximum
VB	Valance Band
CB	Conduction Band
CZO	Zn doped CuO
ZnO:Cu	Cu doped ZnO
VOCs	Volatile Organic Compounds

List of Symbols

Λ	Mean free path
R	Source substrate distance
T	Source temperature
P	Evaporant vapor pressure
P	Chamber pressure
M	Molecular mass of evaporant
R_s	Sheet Resistance
I	Current
V	Voltage drop
CF	Correction factor
F_1	Thickness correction factor
F_2	Geometric dimension
F_3	Edge correction factor
s	Probe spacing
d	Width of the sample
l	Length of the sample
t	Thickness of the sample
n	Carrier concentration
μ	Carrier mobility
λ	Wavelength
θ	Bragg angle
D	Crystallite size
ε	Micro strain
δ	Dislocation density
β	Full width half maximum
ρ	Electrical resistivity
σ	Electrical conductivity
$F(R)$	Kubelka - Munk formula
T	Transmittance
I	Transmitted intensity
I_o	Incident intensity of the light

A	Absorbance
α	Absorption coefficient
R	Reflectance
ν	Frequency
h	Planck's constant
$h\nu$	Photon energy
E_b	Binding Energy
E_k	Kinetic energy
Φ	Work function
ΔE	Activation energy
ΔG	Energy change for chemical reaction
ΔH	Changes in Enthalpy
ΔS	Changes in Entropy
D	Diffusion coefficient of the oxidizing species
F_1	Diffusive flux
C_0	Concentration of the oxidizing species in atmosphere to film surface
C_s	Concentration of the oxidizing species at the $Cu\text{-}Cu_2O$ interface
x	Thickness of the oxide layer
F_2	Reactive flux
K	Reaction rate
S	Sensitivity
R_a	Sensor resistances in air ambient
R_g	Sensor resistances in target gas
C	Concentration of the target gas
e^-	Electron
h^+	Hole

List of Tables

Table 1.1: Brief summary of the operating temperatures of MOs based CO sensors.

Table 3.1: Average grain size for thin copper oxide films of different oxide phase.

Table 3.2: Average grain size of thin CuO films after oxidation at different temperatures in air for 3 hours.

Table 3.3: (a) Binding energy positions and relative peak intensities of de-convoluted O1s and $Cu2p_{3/2}$ spectra of CuO thin films oxidized at 330°C and 600°C, respectively.(b)Relative intensity ratio of O-crst vs $Cu2p_{3/2}$ (total), Cu^+ vs Cu^+ and O-crst vs O-def.

Table 3.4: EDX elemental analysis of samples oxidized for 3hrs at 300°C, 350°C in air and 200°C, 300°C in oxygen ambient.

Table 3.5: Hall data of CuO films, grown at different oxidation temperatures

Table 4.2: Hall data of ZnO thin films grown at different oxidation temperatures for 4hrs

Table 4.1: (a) Binding energy positions and relative peak intensities of deconvoluted O1s and Zn2p spectra of different ZnO thin films. (b) Relative intensity ratio of O-crst vs $Zn2p_{3/2}$ and $Zn2p_{3/2}$ to $Zn2p_{1/2}$

List of Figures

Figure 1.1: Schematic graphical representation of CO impact on human health for different concentration and exposure**.**

Figure 1.2: Schematic representation of various SMO based gas sensor research

Figure 1.3: Schematic representations of gas sensing mechanism for reducing gas: (a) p-type semiconductor and (b) n-type semiconductor.

Figure 1.4: Schematic representation of response curve of (a) p-type and (b) n-type material for CO gas

Figure 1.5: Schematic representation of photo-catalytic dye degradation process.

Figure 1.6: Schematic Representation for photo-generation of electron – hole pairs for Cu_2O, (b) MB dye photo-degradation under visible light.

Figure 2.1: (a) Schematic representation and (b) actual view of thermal evaporation deposition unit.

Figure 2.2: (a) Schematic view of (a) plasma creation and (b) DC/RF magnetron sputtering unit, of a sputter system.

Figure 2.3: (a) Schematics view of rotating crystal X-ray diffraction method with θ-2θ scan, (b) sample mounting state and rotating detector set up and (c) closed chamber X-ray diffractometer.

Figure 2.4: Schematic drawing of (a) field emission scanning electron microscope (FESEM) and (b) interaction of focused electron beam with the matter.

Figure 2.5: (a) Two basic operations (I) diffraction patterns and (II) image formation and (b) schematic view of the transmission electron microscopy.

Figure 2.6: Schematic of scanning tunneling microscopy (STM).

Figure 2.7: (a) Van der Waals force, (b) imaging modes dependence upon the distance between AFM probe and surface of the sample and (c) schematic diagram of atomic force microscope (AFM).

Figure 2.8: Transitions of electrons from valence to conduction band in (a) direct and (b) indirect band gap.

Figure 2.9: Diagram of energy levels for Rayleigh scattering and Raman scattering with Stokes and Anti Stokes line scattering.

Figure 2.10: (a) Photoemission process of electrons and (b) schematic image of X-ray Photoelectron Spectroscopy (XPS).

Figure 2.11: (a) A schematic diagram of (a) four point probe (b) setup image of four probe resistivity measurements.

Figure 2.12: (a) A schematic diagram of four point of Van der Pauw method for rectangular geometric.

Figure 2.13: Schematic view gas sensing measurement system and (b) digital image of measurement setup and vacuum chamber.

Figure 2.14: Schematic side and top views, (b) digital image of metal oxide thin film gas sensor with top Au contacts.

Figure 3.1: Optical photographs of (a) cuprous oxide and (b) cupric oxide thin films grown on glass substrates.

Figure 3.2: Thin Cu films show (a) Temperature dependent sheet resistance in air, (b) R-T measurements of heating and cooling cycles of different Cu films during air annealing (c) comparison of sheet resistance during heating and cooling cycles in air as well as He ambient conditions.

Figure 3.3: XRD spectra (θ - 2θ scan) of thin Cu films after oxidation in air at various temperatures for (I) RT to 350°C for 3hrs durations and (II) 350°C to 600°C for different durations.

Figure 3.4: Schematic representation of grain growth during the oxidation of copper thin films.

Figure 3.5: Crystallite size of CuO_x thin films for different oxide phase.

Figure 3.6: Crystallite size of CuO thin films with oxidation temperatures.

Figure 3.7: XRD spectra of thin Cu films during evolution of Cu_2O oxide phases after oxidation in air at (a) 260°C and (b) 300°C, for different durations. Lorentzian peak fitting of (c-d) Cu(111) and (e-f) Cu2O (111) diffraction lines, along with their oxide growth kinetics shown within the insets.

Figure 3.8: XRD spectra of thin Cu_2O films transformation to CuO oxide phases during thermal oxidation in air at (a) 330°C and (b) 350°C, for different durations. Lorentzian peak fitting of (c-d) Cu_2O (111) and (e-f) CuO (111) diffraction lines.

Figure 3.9: XRD patterns of Cu films of different thickness (100 nm - 300nm) after the oxidation at 150°C for 3hrs.

Figure 3.10: XRD patterns of Cu layers oxidized at oxygen ambient at various temperatures and durations.

Figure 3.11: XRD patterns of Cu layers oxidized at oxygen ambient at various temperatures and durations.

Figure 3.12: Schematic representation of surface oxidation mechanism of thin copper films.

Figure 3.13: SEM image of 400 nm thick Cu films on glass substrate: (a) as-grown (b) oxidized at 300°C, (c) 350°C for 3hrs annealing and (d) 350°C for 9hrs, (e) 500°C for 9hrs, (f) 600°C for 6hrs, (g) 800°C for 2 hrs and (h)1000°C for 2hrs, respectively.

Figure 3.14: SEM image of 400 nm thick Cu films oxidized at 600°C for different duration of annealing (a) 3hrs, (b) 6hrs, (c) 9hrs and (e) 12hrson glass substrate.

Figure 3.15: FESEM images of thermally oxygenized Cu films in oxygen ambient at (a) 200°C for 3 hours for single Cu_2O phase, (b) 300°C for 3 hours for single CuO phase.

Figure 3.16: AFM image of thin Cu films on glass substrate: (a) as-grown (b) oxidized at 300°C and (c) 350°C, respectively, in air ambient.

Figure 3.17: STM images of thin Cu_2O films on glass substrate showing flat islands of triangular shape grown at 300°C. Scan areas (a) 500 nm × 500 nm and (b) 250 nm × 250 nm.

Figure 3.18: Raster spectroscopy of thin Cu_2O films showing flat islands of triangular shape are electronically different from the other surface parts of the STM image. Scan areas (a) 300nm × 300 nm.

Figure 3.19: Raman spectra of various Cu oxides films grown by thermal oxidation of thin Cu films in air. Inset shows the Raman spectrum of Cu film oxidized at 220°C for 4 hours in air.

Figure 3.20: UV-visible spectra of (a) Cu_2O and (b) CuO thin films grown by thermal oxidation in air ambient. Inset shows the optical band gap for different CuOx thin film thicknesses.

Figure 3.21: XPS spectra of different Cu oxide films: (a) Wide Scan (b) Cu2p core level and (c) LMM Auger spectra.

Figure 3.22: XPS spectra of CuO films with different oxidation temperatures: (a) XPS survey Scan of 330°C, 400 and 600°C. High resolution scans for 330°C: (b) O1s and (c) $Cu2p_{3/2.}$ High resolution scans for 600°C: (d) O1s and (e) $Cu2p_{3/2.}$

Figure 3.23: XPS spectra of thermally oxidized thin Cu films in an oxygen ambient condition.

Figure 3.24: EDX spectrum of copper oxide thin film, prepared by 3hrs of oxidation at (a) 300°C (b) 350°C in air ambient and (c) 200°C, (d) 300°C in oxygen ambient.

Figure 3.25: Sheet resistance of thin Cu films (a) I-V plot at room temperature (b) R-T Plots.

Figure 3.26: (a) Rectangular geometry of thin Cu film ($t < s/2$, $a = 2.5$cm and b varies from 7.5 to 2.6 cm) (b) Sheet resistance and(c) G correction factor for thin Cu films of different rectangular geometry as a function of probe spacing (s/b).

Figure 3.27: Schematic representation of the surface electrical resistivity (I-V) measurement (a) top view and (b) cross-sectional view.

Figure 3.28: Surface electrical resistivity (I-V) measurement of CuO films grown at different temperatures for duration of (4hr and (b) 6hr.

Figure 3.29: Comparison of the surface electrical resistivity measurement of CuO thin films for different oxidation temperatures.

Figure 3.30: UV-Vis absorption spectra and (b) MB dye degradations with irradiation time for nano-structured Cu_2O thin film under visible light.

Figure 3.31: (a) UV-Vis absorption spectra and (b) MB dye degradations with irradiation time for nano-structured CuO thin film under visible light.

Figure 3.32: (a) p-type semiconducting behavior and (b) a schematic of response and recovery times of a CuO thin film based sensor in the exposure of CO gas.

Figure 3.33: Variation in sensors response of (a) sample I, (b) sample II, (c) sample III for different concentration and at (d) 50ppm of CO gas as a function of operating temperature (150°C to 250°C).

Figure 3.34: Change in surface electrical resistance due to exposure to various concentrations of CO gas at optimum operating temperatures(a) 230°C for sample I, (b) 250°C for sample II, (c) 280°C for sample III and (d) Sensor operating temperature increases with the oxidation temperatures.

Figure 3.35: The sensors response for different operating temperatures as a function of CO concentration for (a) sample I, sample II, (c) sample III and (d) at optimum operating temperatures for all nano- structured CuO thin films based sensors.

Figure 3.36: Transient behavior of the CuO sensor at optimum temperature (230°C) and 240 ppm indicating response magnitude, response time and recovery time.

Figure 3.37: Surface electrical resistivity (I-V) measurement of CuO sensor samples grown at different oxidation temperatures.

Figure 4.1: Temperature dependent sheet resistance of Zn thin film during annealing in air and helium (He) ambient.

Figure 4.2: XRD spectra of (a, I) as grown Zn thin films and thermally oxidized at temperatures (II) 180°C, (III) 400°C and (b, I) 500°C, (II) 600°C, (III) 650°C and (IV) 700°C for 4hrs.

Figure 4.3: (I) XRD spectra of (a) as-deposited Zn thin films and transformation to ZnO phases for durations of (b) 15min, (c) 30min, (d) 45min and Lorentzian fit of XRD spectra (II) Zn (101) and (III) ZnO(101)diffraction peaks as a function of oxidation time during thermal oxidation in air at 500°C temperature.

Figure 4.4: Area of Zn (101) and ZnO (101) diffraction lines, along with their oxide growth kinetics.

Figure 4.5: FESEM images of Zn films on glass substrate thermally oxidized at: (a & b) as-grown (c & d) 240°C, (e & f) 400°C, (g & h) 500°C and (i & j) 600°C for 4hrs. Right column shows a closer view.

Figure 4.6: FESEM images of Zn Nano-rods on glass substrate. Oxidation temperature: (a & b) 600°C and (c & d) 700°C. Right column shows a closer view.

Figure 4.7: FESEM results of (a) as-grown Zn film and thermally oxidized at (b) 500°C, (c) 600°C, (d) 650°C and (e) 700°C for 4hrs on SiO_2/Si substrate.

Figure.4.8: A schematic representation of different surface morphologies of (a) the transformation of metallic Zn to ZnO phase and (b) ZnO phases at higher temperatures.

Figure.4.9: Schematic representation of different crystal planes of a ZnO nano-rod with prismatic and pyramidal facets

Figure 4.10: Prismatic ZnO nano-rods: (a) SEM image, (b) TEM micrograph, (c) HRTEM image, (d) SAED pattern, and Pyramidal ZnO nano-rod: (e) SEM image (f) TEM micrograph,(g) HRTEM image, (h) SAED pattern.

Figure 4.11: Raman spectra of (a) as grown Zn film and thermal oxidation of Zn films at (b) 180°C, (c) 240°C, (d) 400°C, (e) 500°C, (f) 600°C for 4 hours in air ambient.

Figure 4.12: XPS (a) survey scan and high resolution spectra of (b) O1s, (c) Zn2p binding energy peaks of ZnO nano-rods formed after air oxidation of Zn films at 700°C for 4 hours.

Figure 4.13: High resolution Zn2p and O1s binding energy spectra of ZnO nanostructures grown at different oxidation temperatures.

Figure 4.14: Current – voltage plot of ZnO thin films, prepared at different temperatures during the air annealing.

Figure 4.15: **S**chematic of response and recovery times of a ZnO thin film based sensor in the exposure of CO gas.

Figure 4.16: Responses curve of ZnO nano-rods at different operating temperature (a & d) 200°C, (b & e) 250°C and (c & f) 280°C for various concentrations of CO gas.

Figure 4.17: Response curves of the ZnO nano-porous based sensor at different operating temperature (a & d) 150°C, (b & e) 200°C and (c & f) 250°C for various CO concentrations.

Figure 4.18: Response curves of nano- structured ZnO thin films based sensors at operating temperature 250°C for maximum concentrations of CO gas.

Figure 4.19: Ethanol vapour sensing at the concentration of (a) 2000ppm and (b) 5000ppm of ZnO nano-rods sensor at room temperature.

Figure 5.1: XRD patterns of pure and doped CuO thin films with different concentration of Zn, thermally oxidized at 400°C for 4hrs in air ambient.

Figure 5.2: XRD patterns of (a) pure CuO nano-particles and Zn doped (b) 0.04M, (c) 0.06M, (d) 0.08M of CuO nano-particles.

Figure 5.3: Variation in Crystallite size (D) and micro-strain (ε) of CuO thin films as a function of Zn dopant concentration (power of Zn target)

Figure 5.4: FESEM results of (a) pure and doped CuO_x thin films with different concentration of Zn (b) Zn@50W, (c) Zn@80W, deposited using sputtering method and then thermally oxidized at 400°C for 4hrs on glass substrate.

Figure 5.5: FESEM results of (a) pure CuO nano-particles (b)CuO-ZnO nano-composite with 0.08M concentration of Zn.

Figure 5.6: (a) UV-visible absorption spectra, (b) Energy band gap [$(\alpha h\upsilon)^2$ vs. hυ] plot and (c) variation of the band gap with Zn concentration of pure and Zn doped CuO nano-particles

Figure 5.7: Raman spectra of (a) pure and doped CuO_x thin films with the power of Zn target are (b) 30W and 40W, (c) 50W and 60W, (d) 70Wand 80W.

Figure 5.8: Raman spectra of (a) pure and doped CuO_x nano-particles (b) 0.04M, (c) 0.06M and (d) 0.08M)

Figure 5.9: XPS survey scans sputter grown doped Zn:CuO films with various Zn concentrations (using Al-K_α line).

Figure 5.10: XPS survey scans sputter grown doped Zn:CuO films with various Zn concentrations (using Mg-K_α line).

Figure 5.11: A schematic of the bar graph for different phases of ZnO:CuO mixed oxides (a) Physical growth route through sputter deposition and (b) Chemical growth route through sol-gel synthesis.

Flow Chart I

Semi-conductors Metal Oxide (SMO)

Preparation

Physical Route under Vacuum

Thermal evaporation

Sputtering

RF/DC Sputtering

Oxidation

Electrical

Structural

Optical

Chemical

Surface Morphology

Applications

Flow Chart II

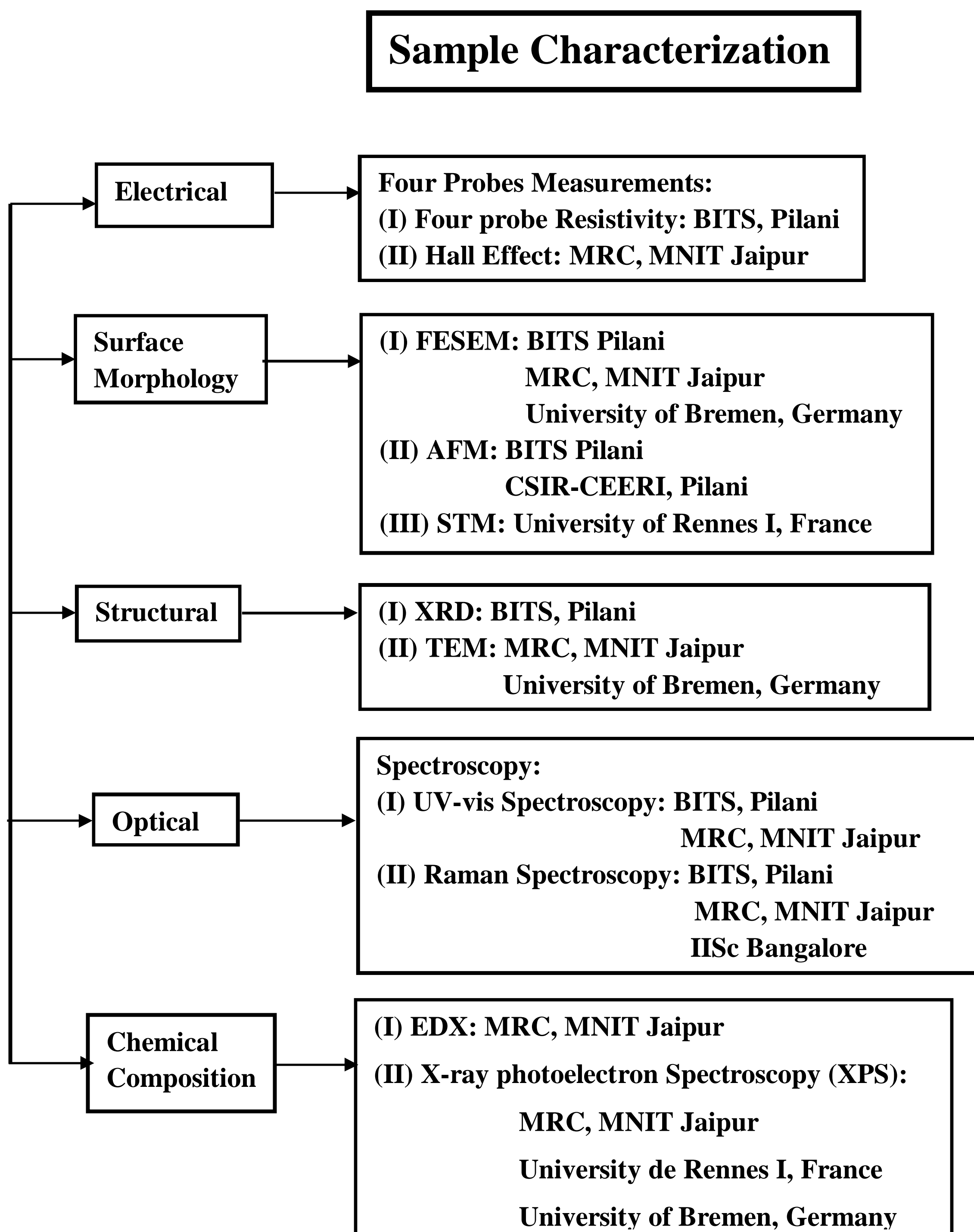

Flow Chart III